Nonlinear sound-sheet microscopy

Imaging opaque organs at the capillary and cellular scale

Heiles, Baptiste; Nelissen, Flora; Waasdorp, Rick; Terwiel, Dion; Park, Byung Min; Ibarra, Eleonora Munoz; Matalliotakis, Agisilaos; Ara, Tarannum; Barturen-Larrea, Pierina; Duan, Mengtong

DOI
10.1126/science.ads1325

Publication date
2025

Document Version
Final published version

Published in
Science (New York, N.Y.)

Citation (APA)
Heiles, B., Nelissen, F., Waasdorp, R., Terwiel, D., Park, B. M., Ibarra, E. M., Matalliotakis, A., Ara, T., Barturen-Larrea, P., Duan, M., Shapiro, M. G., Gazzola, V., & Maresca, D. (2025). Nonlinear sound-sheet microscopy: Imaging opaque organs at the capillary and cellular scale. *Science (New York, N.Y.)*, *388*(6742), Article eads1325. https://doi.org/10.1126/science.ads1325

RESEARCH ARTICLE SUMMARY

ULTRASOUND IMAGING

Nonlinear sound-sheet microscopy: Imaging opaque organs at the capillary and cellular scale

Baptiste Heiles, Flora Nelissen, Rick Waasdorp, Dion Terwiel, Byung Min Park, Eleonora Munoz Ibarra, Agisilaos Matalliotakis, Tarannum Ara, Pierina Barturen-Larrea, Mengtong Duan, Mikhail G. Shapiro, Valeria Gazzola, David Maresca*

INTRODUCTION: Enabling discoveries in the field of biology often requires new ways of visualization. One of the most informative methods for observing dynamic cellular processes in living organisms uses light-sheet microscopy to leverage genetically encoded fluorescent reporters. Unfortunately, optical microscopy is phototoxic to cells and remains restricted to the study of thin transparent specimens. The physics of high-frequency ultrasound is ideally suited to in vivo cellular imaging by providing a combination of deep penetration (~1 cm) and high spatiotemporal resolution (~100 μm, 1 ms). In addition, the recent introduction of genetically encoded gas vesicles (GVs) as the "green fluorescent protein for ultrasound" creates new opportunities for in vivo studies of cellular function. To equip ultrasound with capabilities analogous to those given to optical microscopy by fluorescent proteins, there is a need for fast high-resolution and volumetric ultrasound imaging methods capable of visualizing acoustic reporter genes and acoustic biosensors. If this can be achieved, the resulting capabilities will allow researchers to explore previously inaccessible cellular biology in vivo with unparalleled information content, resolution, coverage, and translatability to biological research and clinical development.

RATIONALE: We introduce the concept of nonlinear sound-sheet microscopy (NSSM), a method capable of detecting both genetically encoded GVs and synthetic lipid-shelled microbubbles (MBs) across thin living tissue sections. The fundamental idea behind this method is to modulate acoustic pressure along the main lobe of nondiffractive ultrasound beams to confine the nonlinear scattering of GVs and MBs to thin tissue sections. Because GVs and MBs respond to increasing acoustic pressure levels in a nonlinear way, they can be distinguished from surrounding tissues that respond to increasing pressure levels in a linear way. To maximize the volumetric field of view of NSSM, we developed our imaging method on a class of high-frequency ultrasound transducers called row-column–addressed (RCA) arrays. In our current implementation, the imaging field of view was approximately 1 cm^3.

RESULTS: Firstly, we assessed the capacity of NSSM to detect bacterial acoustic reporter genes in three dimensions. *Escherichia coli* engineered to constitutively express nonlinearly scattering GVs were successfully detected along the two orthogonal directions of a 15-MHz RCA array. By sweeping electronically the sound-sheet plane along the two orthogonal directions of the RCA array, we captured volumetric images of bacterial acoustic reporter genes spanning 8.8 × 8.8 × 10 mm^3. Secondly, we performed longitudinal NSSM of genetically labeled tumors and revealed three-dimensional (3D) patterns of GV expression over several days. We showed that NSSM can be used to track tumor growth but also to quantify both tumor and necrotic core volumes. Thirdly, we demonstrated that NSSM is capable of detecting synthetic lipid-shelled MBs, a class of resonant ultrasound contrast agents used as vascular reporters. Using NSSM at kilohertz frame rates in arbitrarily selected planes, we acquired nonlinear Doppler images of the rat brain vasculature across the entire brain. Lastly, the combination of NSSM with ultrasound localization microscopy allowed us to map cerebral blood flows below 3 mm/s, thereby revealing the capillary vasculature in living rat brains in 100-μm-thick tissue sections.

CONCLUSION: We demonstrated the ability of NSSM to confine nonlinear scattering of genetically encoded GVs and synthetic lipid-shelled MBs to wavelength-thin opaque tissue sections. NSSM is an imaging method that can either be tuned for speed or coverage. In two dimensions and at an ultrasound frequency of 15 MHz, NSSM can scan 1 cm deep with a theoretical frame rate of 25.6 kHz. In three dimensions, NSSM can acquire 8.8 × 8.8 × 10 mm^3 volumes of tissue with a theoretical volume rate of 233 Hz. To use NSSM to the fullest, new generations of brighter acoustic reporter genes and faster biosensors will have to be developed. Additionally, the sensitivity of NSSM should be improved further to enable single-cell detection. If we are successful, NSSM will carry a wave of opportunities for dynamic imaging studies of biological processes across scales. ■

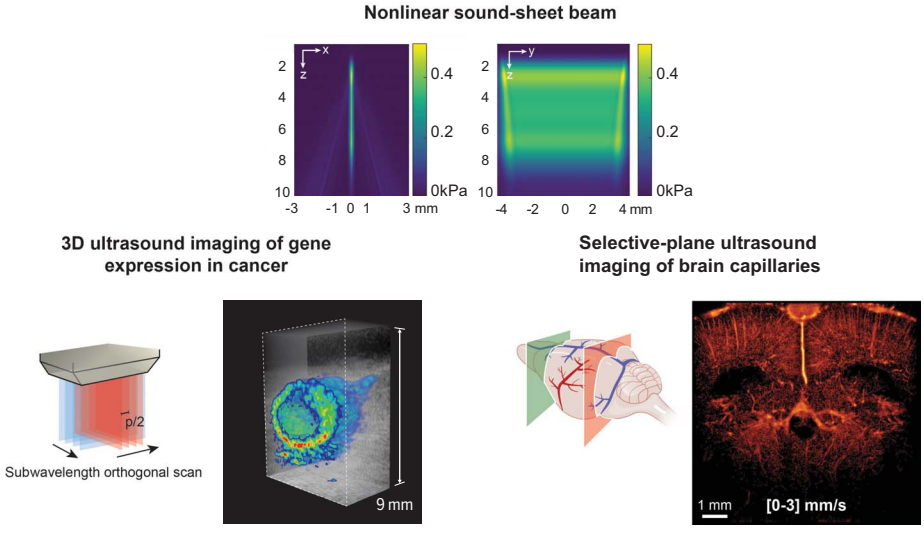

Nonlinear sound-sheet microscopy. The ability to excite acoustic reporters one plane at a time enables molecular ultrasound imaging at the cellular and capillary scales. (i) In NSSM, the nonlinear scattering of acoustic reporters is confined to thin sound sheets spanning 0.1 × 10 × 9 mm^3. (ii) Orthogonally swept sound-sheet imaging enables the 3D visualization of gene expression in opaque organs, whereas (iii) sound-sheet localization microscopy enables deep super-resolution imaging of brain capillaries. *p*, pitch of the RCA. *p*/2 was equal to 55 μm in this study.

The list of author affiliations is available in the full article online.
*Corresponding author. Email: d.maresca@tudelft.nl
Cite this article as B. Heiles *et al.*, *Science* **388**, eads1325 (2025). DOI: 10.1126/science.ads1325

READ THE FULL ARTICLE AT
https://doi.org/10.1126/science.ads1325

RESEARCH ARTICLE

ULTRASOUND IMAGING

Nonlinear sound-sheet microscopy: Imaging opaque organs at the capillary and cellular scale

Baptiste Heiles[1]†, Flora Nelissen[2], Rick Waasdorp[1], Dion Terwiel[1], Byung Min Park[1], Eleonora Munoz Ibarra[1], Agisilaos Matalliotakis[1], Tarannum Ara[1], Pierina Barturen-Larrea[3], Mengtong Duan[3], Mikhail G. Shapiro[3,4,5], Valeria Gazzola[2,6], David Maresca[1]*

Light-sheet fluorescence microscopy has revolutionized biology by visualizing dynamic cellular processes in three dimensions. However, light scattering in thick tissue and photobleaching of fluorescent reporters limit this method to studying thin or translucent specimens. In this study, we applied nondiffractive ultrasound beams in conjunction with a cross-amplitude modulation sequence and nonlinear acoustic reporters to enable fast and volumetric imaging of targeted biological functions. We reported volumetric imaging of tumor gene expression at the cubic centimeter scale using genetically encoded gas vesicles and localization microscopy of cerebral capillary networks using intravascular microbubble contrast agents. Nonlinear sound-sheet microscopy provides a ~64× acceleration in imaging speed, ~35× increase in imaged volume, and ~4× increase in classical imaging resolution compared with the state of the art in biomolecular ultrasound.

The most informative method for observing dynamic cellular processes in vivo in three dimensions uses light-sheet microscopy that leverages genetically encoded fluorescent reporters (*1*). Successive advances in light-sheet microscopy now enable fast, large-volume, and high-resolution imaging of fluorescently labeled cells in transparent or cleared organisms (*2*, *3*). These capabilities have had a tremendous impact, for example, in developmental biology by enabling long-term imaging of embryogenesis (*4*–*7*).

A next frontier would be to achieve nontoxic deep-tissue imaging with cellular precision in living opaque organisms. Unfortunately, limitations inherent to optical microscopy (penetration depth < 1 mm and phototoxicity) (*8*, *9*) prevent large-scale imaging in opaque tissue. In addition, fast light-sheet imaging (*2*) does not yet reach 1 mm^3/s volume rates in living tissue (*10*), which makes dynamic imaging at the mesoscale (*11*) technically challenging.

The introduction of biogenic gas vesicles (GVs) (*12*) as the "green fluorescent protein for ultrasound" provides an alternative to light for large-scale cellular imaging. The fortuitous physics of ultrasound enables centimeters-deep scanning of mammalian tissue, whereas genetically encoded GVs can interface ultrasound waves with cellular function (*13*, *14*). To unlock the potential of GV-based acoustic reporter genes (ARGs) (*15*, *16*) and biosensors (*17*), there is a need for ultrasound imaging methods with high information content, resolution, coverage, and translatability. Recently, four-dimensional (4D) functional ultrasound neuroimaging (*18*, *19*) and 3D ultrasound localization microscopy (*20*) have positioned ultrasound as a tool for basic biology research. However, it remains difficult to visualize cellular function in three dimensions or to detect capillary networks.

In this study, we introduce nonlinear sound-sheet microscopy (NSSM), a method to image targeted biological functions across cubic centimeters of opaque living tissue. NSSM relies on a large–field of view, high-frequency row-column–addressed transducer array (RCA) (*21*–*23*) and the transmission of nondiffracting ultrasound beams to detect cells labeled with GVs (*24*) or vessels labeled with microbubbles (MBs) (*25*). NSSM expands the field of view of biomolecular ultrasound at 15 MHz (*24*, *26*–*28*) from ~3.5 × 64 × 100 λ^3 to 80 × 80 × 100 λ^3 (where λ denotes the ultrasound wavelength), the upper bound 2D imaging speed from 400 to 25.6 kHz, and spatial resolution from 1 × 1 × 3.5 λ^3 to 1 × 1 × 0.6 λ^3. We demonstrate the versatility of NSSM by performing volumetric imaging of gene expression in a cancer model, and nonlinear acoustic sectioning of the living cerebral vasculature down to the capillary scale. Throughout the study, NSSM is compared to linear imaging as reference.

Concept

In the NSSM paradigm, a subaperture of RCA transducer elements N_{ap} (Fig. 1A) is used to transmit cross-propagating ultrasound plane waves, or X waves, from two adjacent half-apertures at α and −α angles (Fig. 1B). This spatially structured ultrasound transmission gives rise to a nondiffractive acoustic pressure field in the *xz* plane (*29*) exhibiting a double acoustic pressure along the main lobe of the beam as well as a plane wave acoustic pressure field in the *yz* plane (*30*) (Fig. 1C). Acoustic pressure is further modulated along the main lobe of the nondiffractive beam by using a cross-amplitude modulation (xAM) pulse sequence (*24*) (Fig. 1D), which confines nonlinear scattering to a thin sound sheet with a constant beam width, regardless of depth (Fig. 1E). The sound sheet beam extends up to the cross-propagation depth $z_{cp} = \frac{N_{ap}}{2}\cot\alpha$, which is typically of the order of 100λ. 2D images are reconstructed from backscattered ultrasound echoes received on elements of the orthogonal RCA array (Fig. 1B) by using a delay-and-sum beam-forming algorithm (see materials and methods). The point spread functions (PSFs) of resonant MBs are reported (Fig. 1F) for linear imaging or SSM [i.e., transmission event 1 (TX1) only] and NSSM (i.e.,TX1-TX2-TX3). We chose MBs as nonlinear point targets in simulation rather than GVs because equations governing their vibration in an ultrasound field are known. SSM and NSSM images in the *xz* plane showed similar PSFs because both imaging modes operate at the same frequency (Fig. 1G). To scan a volume, sound-sheet transmissions were swept electronically along the two arrays of the RCA transducer by using a sliding aperture of elements (Fig. 1H). A ~λ/2 microscanning precision was achieved by interleaving transmissions with and without a silent element at the center of the subaperture (Fig. 1H) because the pitch *p* or interelement spacing of the RCA was approximately equal to λ. 3D PSFs are reported in Fig. 1I. Nonlinear imaging reduced the 3D PSF secondary lobe levels by 12.8 ± 4.4 dB thanks to the confinement of nonlinear MB scattering to the sound-sheet plane. In terms of resolution, NSSM delivered an average 3D point spread function of 1 × 0.6 × 0.6 λ^3 compared with 1 × 0.9 × 0.9 λ^3 for SSM (Fig. 1J). Additional data supporting Fig. 1 are provided in the materials and methods section and fig. S1.

Volumetric NSSM of gene expression at the cubic centimeter scale

Nonlinear ultrasound imaging is key to detect GVs in a tissue context with high specificity (*24*). To test the ability of NSSM to visualize gene expression in three dimensions, we first imaged GVs adapted as nonlinear bacterial ARGs (*15*, *28*) (Fig. 2). We purified *Anabaena flos-aquae* GVs and embedded them in acoustically transparent phantoms at concentrations ranging from optical densities at λ = 500 nm (OD_{500}) of 0.5 to 2, thereby mimicking increasing expression levels in cells (*15*) (Fig. 2A). The phantom was scanned with an orthogonal NSSM sequence by using a 55-μm scanning step.

[1]Department of Imaging Physics, Delft University of Technology, Delft, Netherlands. [2]Netherlands Institute for Neuroscience, Amsterdam, Netherlands. [3]Division of Chemistry and Chemical Engineering, California Institute of Technology, Pasadena, CA, USA. [4]Andrew and Peggy Cherng Department of Medical Engineering, California Institute of Technology, Pasadena, CA, USA. [5]Howard Hughes Medical Institute, Pasadena, CA, USA. [6]Department of Psychology, University of Amsterdam, Amsterdam, Netherlands.
*Corresponding author. Email: d.maresca@tudelft.nl
†Present address: Division of Chemistry and Chemical Engineering, California Institute of Technology, Pasadena, CA, USA.

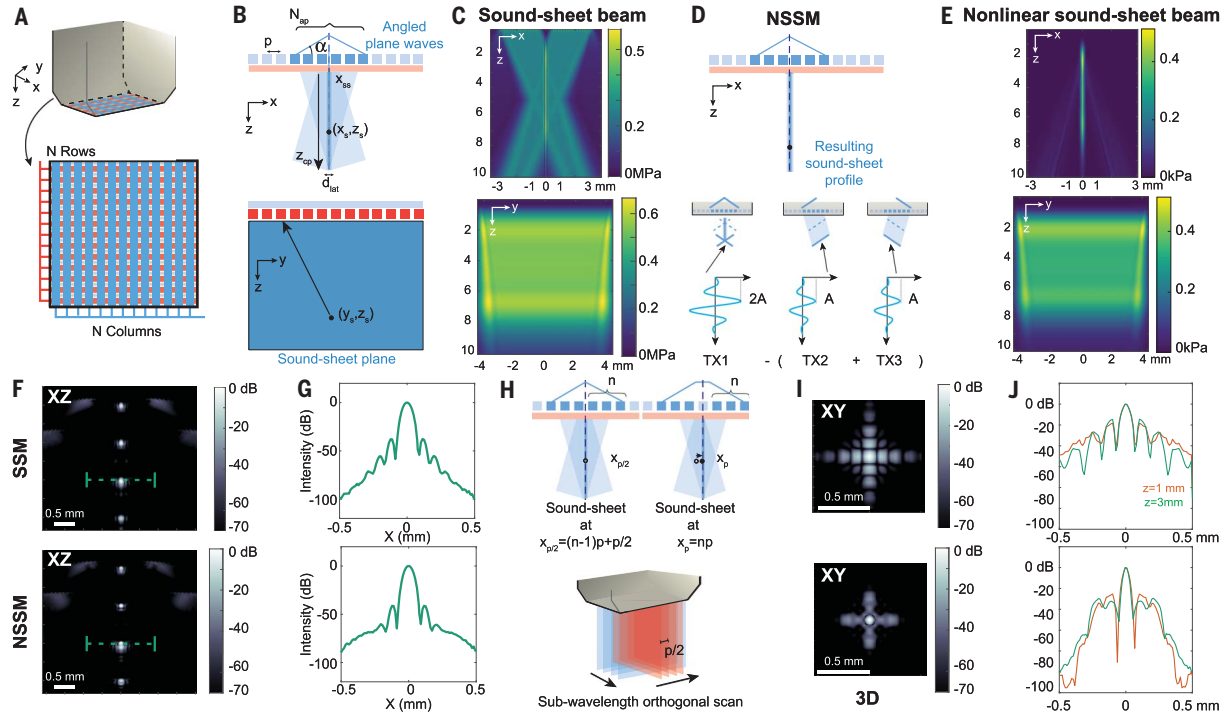

Fig. 1. Concept of NSSM. (**A**) RCA design featuring long and thin transducer elements arranged as rows (red) and columns (blue). (**B**) (Top) X-wave transmission with a subaperture of column elements. d_{lat}, representative width of the sound sheet. (Bottom) Reception of backscattered echoes with row elements. (**C**) Simulated X-wave acoustic pressure fields in the *xz* and *yz* direction. (**D**) (Top) Spatial confinement nonlinear ultrasound intensity along the main lobe of the X-wave beam using a xAM pulse sequence. (Bottom) Three pulses of the xAM sequence that modulate acoustic pressure *A* along the main lobe of the X-wave beam. (**E**) Simulated residual acoustic pressure field resulting from the xAM sequence in a homogeneous nonlinear water medium. (**F**) Simulated images of four resonant MBs in a water medium. (Top) SSM image obtained from transmit event TX1. (Bottom) NSSM image obtained from all transmissions of the xAM sequence. (**G**) SSM (top) and NSSM (bottom) intensity profiles through a resonant MB. (**H**) (Top) Electronic sound-sheet microscanning along one array of the RCA. $x_{p/2}$, sound sheet position between two RCA elements. (Bottom) Orthogonal sound-sheet microscanning process. (**I**) SSM (top) and NSSM (bottom) orthogonally scanned PSFs of a resonant MB in the *xy* plane. (**J**) SSM (top) and NSSM (bottom) intensity profiles through the center of the first and third MBs in the *x* direction.

SSM detected GV wells at all concentrations (Fig. 2B) and normalized contrast-to-noise ratios (CNRs) scaled by steps of 6.9 dB on average from −20.8 dB for OD = 0.5 to 0 dB for OD = 2. NSSM detected GV wells at all concentrations (Fig. 2C) and exhibited a larger, 33-dB dynamic range between the GV well at OD = 0.5 and the GV well at OD = 2. We observed a lower increase in CNR from OD = 1.5 to OD = 2, possibly owing to pressure-dependent ultrasound attenuation in a medium containing buckling GVs (*31*). Additional results for linearly and nonlinearly scattering purified *A. flos-aquae* GVs are reported in fig. S2. A representative dataset can be found online (*32*).

Next, we tested the ability of NSSM to visualize bacterial ARG expression, which is of particular interest for the field of engineered bacterial biosensors (*33*) and therapeutics (*27*, *28*). Two different strains of *Escherichia coli* were used, a control strain and a strain transfected with plasmid pBAD-bARGSer (*28*), the latter leading to intracellular production of *Serratia* GVs, which constitutively produce nonlinear scattering (Fig. 2D). Both strains of bacteria were embedded in agar phantoms and imaged with NSSM (Fig. 2E). Imaging volumes of 8.8 × 8.8 × 10 mm^3 were reconstructed from 108 sound-sheet scanning positions of the RCA transducer (Fig. 2G). As expected, the control strain did not show any nonlinear contrast, whereas bacteria expressing *Serratia* GVs were detected both in two and three dimensions (Fig. 2, E to G). NSSM detected nonlinear bacterial ARGs with a CNR of 27 dB.

Longitudinal NSSM of genetically labeled tumor cells

To go further, we investigated the ability of NSSM to image mammalian ARGs (mARGs) in a mouse model of cancer. Orthotopic tumors were induced bilaterally in the mammary fat pads of female immunocompromised mice by injecting cancer cells engineered to produce nonlinearly scattering GVs (*28*) (Fig. 3A). In vivo mARG expression was induced by doxycycline injections every day until day 4 or 8. Tumors were imaged at day 4 after induction in three mice and at day 8 after induction in two mice. A representative dataset can be found online (*32*).

Whereas SSM images revealed anatomical structures, including tumor masses, NSSM successfully revealed spatial patterns of mARG expression within these tumor masses (results of Fig. 3B are also provided in fig. S3 with an equal dynamic range and identical colormap). At day 8 after induction, NSSM revealed the necrotic core of breast tumors through the absence of gene expression. The high specificity of NSSM (*24*), which is robust to nonlinear wave propagation artifacts, was key for this experimental observation. Volumetric imaging enabled us to display cross-sectional views of mARG expression in the *xy* plane, referred to as a C-scan (Fig. 3B, right). Tumors were clearly detected at both stages, but necrotic cores were only visible at day 8 after induction.

Volumetric NSSM fused with anatomical SSM imaging is reported in Fig. 3C. The total volume scanned extends across 8.8 × 8.8 × 9 mm^3 and was acquired with a scanning step of 55 μm along each array of the RCA transducer.

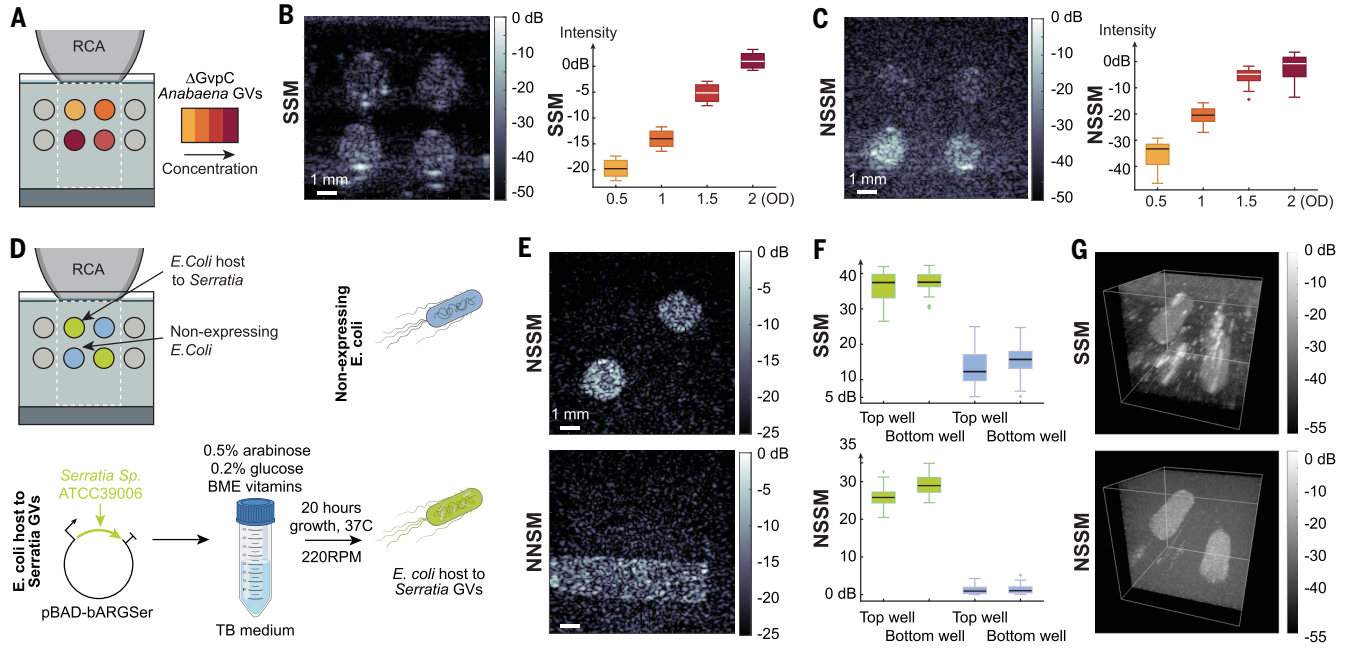

Fig. 2. Large-volume NSSM of bacterial ARGs. (**A**) Experimental setup showing the RCA transducer in contact with an agar phantom (gray) containing wells filled with increasing concentrations *A. flos aquae* GVs stripped of the shell-stiffening protein GvpC to exhibit nonlinear ultrasound scattering. The RCA field of view is indicated in dashed white lines. (**B**) (Left) SSM image for an angle α = 19°. (Right) CNR of each well as a function of the GV OD. (**C**) (Left) NSSM image corresponding to (B). (Right) CNR of each well as a function of the GV OD. (**D**) Experimental setup with wells containing two strains of *E. coli* bacteria, wild-type *E. coli* (blue) and GV-expressing *E. coli*. (green). See protocol (*28*) for bacterial ARG expression. (**E**) Short- and long-axis NSSM images obtained with rows and columns of the RCA, respectively. (**F**) SSM and NSSM CNRs measured out of 108 sound-sheet positions across the GV wells. The blue and green boxes correspond to CNR measured for respectively nonexpressing *E. coli* bacteria and *E. coli* expressing *Serratia* GVs. (**G**) 8.8 × 8.8 × 10 mm^3 volumetric SSM and NSSM images of the phantom.

Figure 3C displays cross-sectional views of gene expression in *xz*, *yz*, and *xy* planes, illustrating 3D navigation capabilities of NSSM. We quantified tumor and necrotic core volumes using a custom automatic segmentation pipeline (Fig. 3D). At day 4 after induction, volumes measured with and without necrotic cores were similar, whereas at day 8 after induction, volumes measured with and without necrotic cores showed a statistically significant difference. A representative automatic segmentation of tumor gene expression contours is provided in Fig. 3D. In these deep-tissue imaging experiments, in vivo patterns of gene expression remained quasistatic because the breathing rate of anesthetized mice was ~60 breaths/min. We chose to operate orthogonally scanned volumetric NSSM at 4 volumes/s, which was enough to prevent breathing motion artifacts. Note that in imaging scenarios that would require higher volume rates, such as imaging of calcium signaling, 3D NSSM could reach 200 volumes/s (table S1). The quantification of in vivo tumor volumes would have been impossible based on anatomical ultrasound imaging alone, which highlights the potential of this imaging method.

Ultrasound sectioning of the brain vasculature with Doppler NSSM

Alongside genetically encoded GVs, synthetic lipid-shelled MBs are another class of ultrasound contrast agents used as vascular reporters. MBs exhibit amplitude-dependent ultrasound scattering (*34*), which makes them detectable with amplitude modulation pulse sequences as well (*25*, *35*). To test the capacity of NSSM to visualize MBs circulating in blood vessels, we performed high-speed nonlinear Doppler imaging of the rat brain vasculature (Fig. 4).

MBs tuned for high-frequency ultrasound were administered via tail vein injections in anesthetized head-fixed rats (Fig. 4A). As a reference, linear Doppler SSM images were acquired at a 4.4-kHz frame rate (Fig. 4B) and generated results similar to ultrafast Doppler images of the rat brain (*36*). Doppler NSSM images (Fig. 4C) were obtained by using amplitude-modulated data and a high-pass filter to remove residual static echoes (see materials and methods). Note that nonlinear Doppler results did not rely on any singular value decomposition (SVD) filter (*37*). Because nonlinear Doppler processing spatially confines image data to a 0.1 × 9.6 × 8.8 mm^3 thin sound-sheet plane, we detected fewer vessels in Fig. 4C than in Fig. 4B, which projects in one image echoes arising from the oblique paths of each plane wave (Fig. 1C). As a result, the cortical surface was clearly delineated in Doppler NSSM (Fig. 4C), whereas vascular signals projected from the oblique paths of each plane wave were visible above the cortex in Fig. 4B. Figure S4 shows that Doppler NSSM is more sensitive to slow blood flows than Doppler SSM based on SVD filtering, which is in line with previous observations (*38*).

Next, we performed ultrasound sectioning of the rat brain vasculature with subwavelength scanning steps of 55 μm (Fig. 4D), acquiring four consecutive Doppler acquisitions per plane. We assessed vascular changes quantitatively in these adjacent planes by computing structural similarity index matrix values for each Doppler acquisition (Fig. 4E). Within sets, the structural similarity index averaged to 0.99, indicating that vascular images were nearly identical across cardiac cycles. Between sets, the index dropped to 0.96, confirming that we observed two separate vascular planes.

Inspired by multislice tomography techniques, we tested the ability of Doppler NSSM to capture multiple views of the brain simultaneously. To do so, we interleaved pulse sequence transmission using two subapertures of elements of the array (Fig. 4F and fig. S5) because RCA arrays cannot discriminate echoes arising from two different planes in reception. In this configuration, we set our imaging rate to 1.7 kHz in both sound-sheet planes. To demonstrate the versatility of this approach, we imaged two coronal vascular planes separated by 3.3 mm using the first array of the RCA transducer (Fig. 4G). Similarly, we imaged two sagittal vascular planes separated by 3.3 mm using the second array of

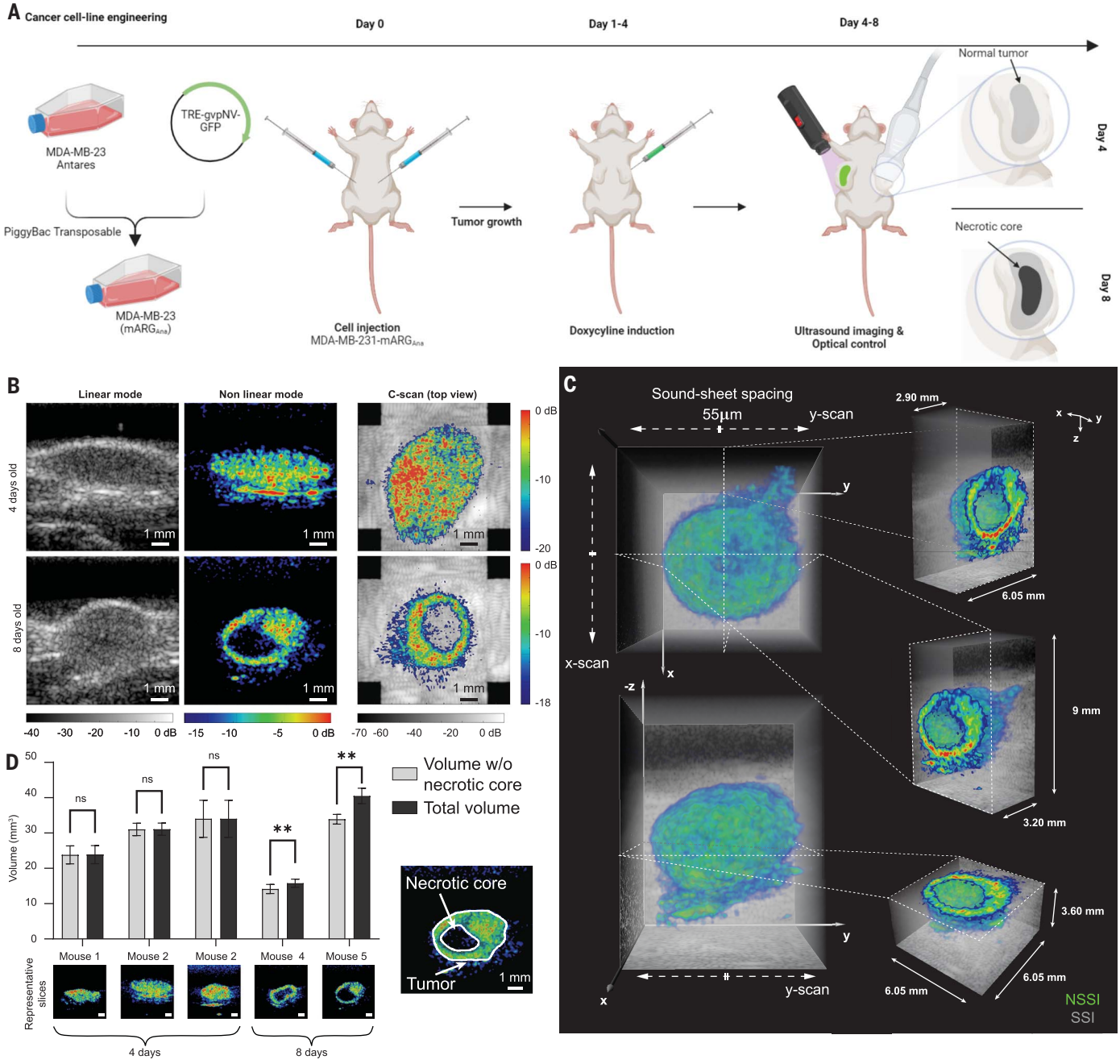

Fig. 3. Longitudinal NSSM of tumor gene expression. (**A**) Protocol for ultrasound imaging of mARG expression in orthopic tumors (see materials and methods). [Figure created with BioRender.com] (**B**) (Left) SSM images of 4- and 8-day-old tumors. (Middle), NSSM images revealing mARG expression in tumors. (Right) *xy* image of an orthogonal 3D NSSM scan overlaid on linear imaging data. Scale bars, 1 mm. (**C**) Representative 3D NSSM of an 8-day-old tumor overlaid on the grayscale SSM volume. (**D**) (Top left) Results of an automatic segmentation (tissue attenuation compensation, followed by 3D Gaussian filtering, 2D binarization using Otsu's method for thresholding, and area measurement using connected components) of the tumor and necrotic core for five mice. The 2D segmentation is performed in each of the scanned direction of the sound sheets and in the transverse direction on the compounded volume (three data points per animal). Light gray plots the tumor volume without the necrotic core, and dark gray plots the tumor volume including the necrotic core (multiple paired *t* test; $^{**}P < 0.01$). (Bottom left) Representative 2D NSSMs of the tumors for each mouse are shown. Scale bars, 1 mm. (Right) Automatic segmentation result at day 8.

the RCA transducer, revealing symmetric vascular planes in each hemisphere (Fig. 4H). Lastly, we processed SSM Doppler spectrograms in each sagittal plane to show that acquisitions were continuous and coregistered in time (Fig. 4, I and J, and fig. S6). The Doppler-derived heart-rates were equal to 298 and 295 bpm in left and right brain hemispheres.

NSSLM reveals the brain capillary vasculature

In 2015, vascular ultrasound was redefined by the introduction of ultrasound localization microscopy (ULM), a super-resolution method that can map the in vivo microvasculature with a ~λ/8 resolution (*39*). A drawback of current ULM processing is that SVD-based filters used to isolate MB echoes are unable to detect slowest blood flow velocities occurring in capillary

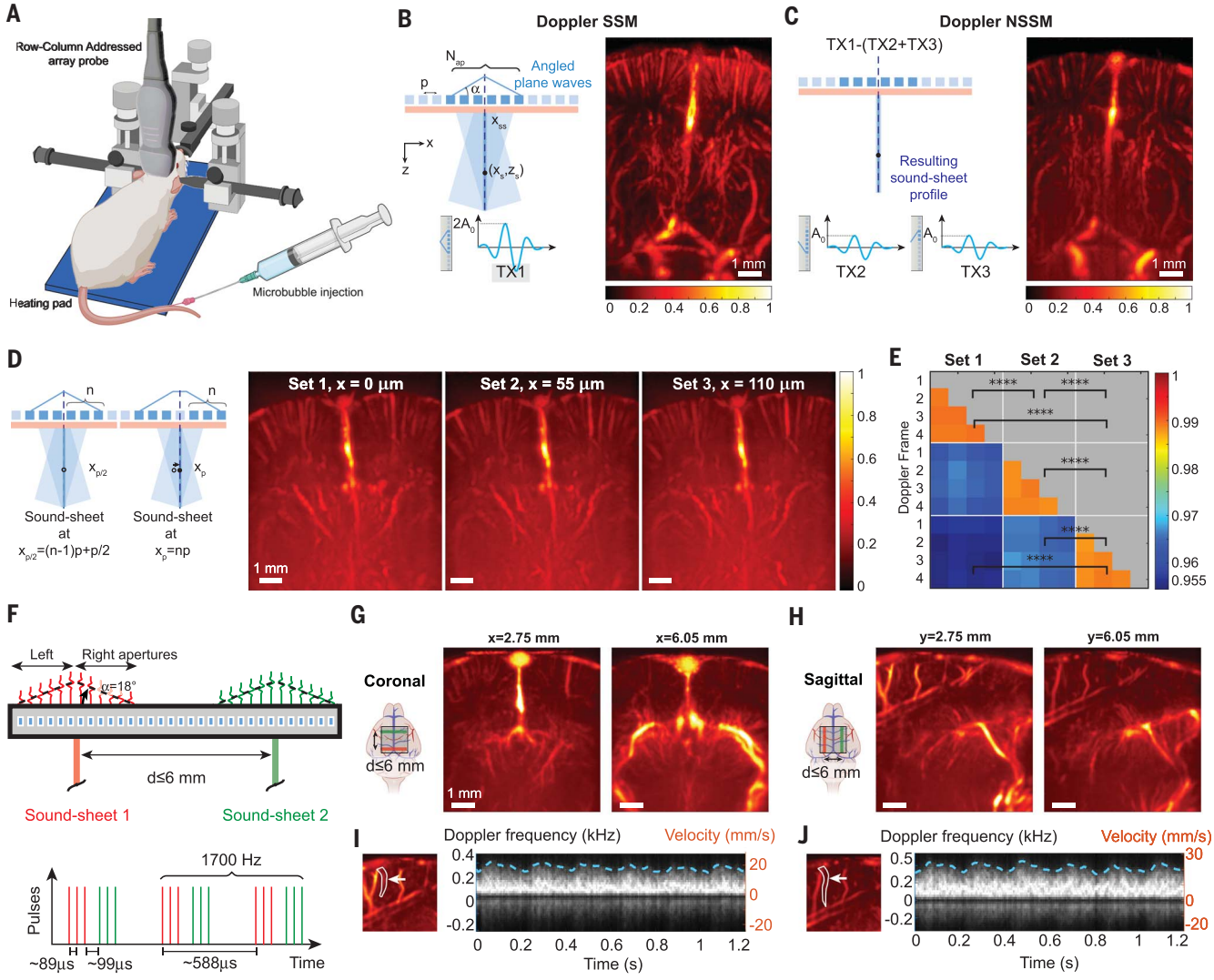

Fig. 4. High-speed multiview NSSM of the rat brain vasculature. (**A**) Experimental setup. (**B**) Coronal section of the rat brain vasculature acquired with 4.4-kHz Doppler SSM after MB injection from 2100 images. (**C**) Same brain section as in (B) acquired with 4.4-kHz Doppler NSSM after MB injection from 2100 images. (**D**) Doppler NSSM of three adjacent coronal brain sections with a 55-µm microscanning step. (**E**) SSIM calculated using four Doppler NSSM acquisitions in each of the three adjacent planes. Asterisks show statistical significance using *t* test of two independent samples (*P* values < 10^{-21}; ***P < 0.001; ****P < 0.0001). (**F**) Multiview NSSM imaging principle using two sub-aperture elements of the RCA transducer. With our RCA probe, imaging planes can be spaced up to 6 mm, and imaging speed was set to 1.7 kHz per plane. (**G**) High-speed multiview Doppler NSSM of two coronal planes. (**H**) High-speed multiview Doppler NSSM of two symmetric sagittal planes. (**I**) Doppler spectrum revealing peak cerebral blood flow and pulsatility of a cortical arteriole of the left hemisphere. (**J**) Doppler spectrum revealing peak cerebral blood flow and pulsatility of a cortical arteriole of the right hemisphere.

beds (*38*, *40*). Consequently, ULM has not been able to visualize capillaries despite capillaries representing the largest vascular territory of living organisms (*41*). Because the NSSM detection of MBs relies on nonlinear MB scattering rather than MB motion, we hypothesized that the combination of NSSM and ULM could potentially reveal capillary beds in vivo.

We investigated nonlinear sound-sheet localization microscopy (NSSLM) of the cerebral capillary vasculature in Fig. 5. Craniotomized rat brains perfused with MBs were imaged at 1 kHz using NSSM in a coronal midbrain plane over the course of 105 s, leading to the acquisition of 10^5 frames (Fig. 5A). Two independent postprocessing pipelines were used to generate state-of-the-art ULM images and NSSLM images. For NSSLM, signal processing first consisted of filtering MB echoes with the amplitude modulation step of NSSM. Secondly, and to increase the signal-to-noise ratio and compensate for attenuation, the one-lag cross-correlation of the AM signal was computed and the signal was further adjusted using an adaptive time gain compensation function. To remove residual nonlinear tissue signals, a singular value decomposition clutter filter was applied with a cutoff of one singular value. Lastly, a 3D fast Fourier transform (FFT) fan filter was implemented, and the signal was decomposed in the following velocity bands: 0 to 3, 3 to 15, 15 to 25, 25 to 60, and 60 to 150 mm/s. The imaging dataset was transformed back to the spatio-temporal domain, and MBs were localized by using the radial symmetry algorithm (*42*). Individual MBs were paired with the Kuhn-Munkres (*43*) assignment to retrieve MB trajectories.

Figure 5B displays SSM Doppler and NSSM Doppler images filtered in the capillary flow velocity band (0.5 to 3 mm/s) (*44*, *45*), showing that NSSM retrieves vascular signals in cortical and hippocampal regions of the rat brain with a good SNR, whereas the SSM images are mostly filled with diffuse vascular noise. In particular, low velocities located at the wall

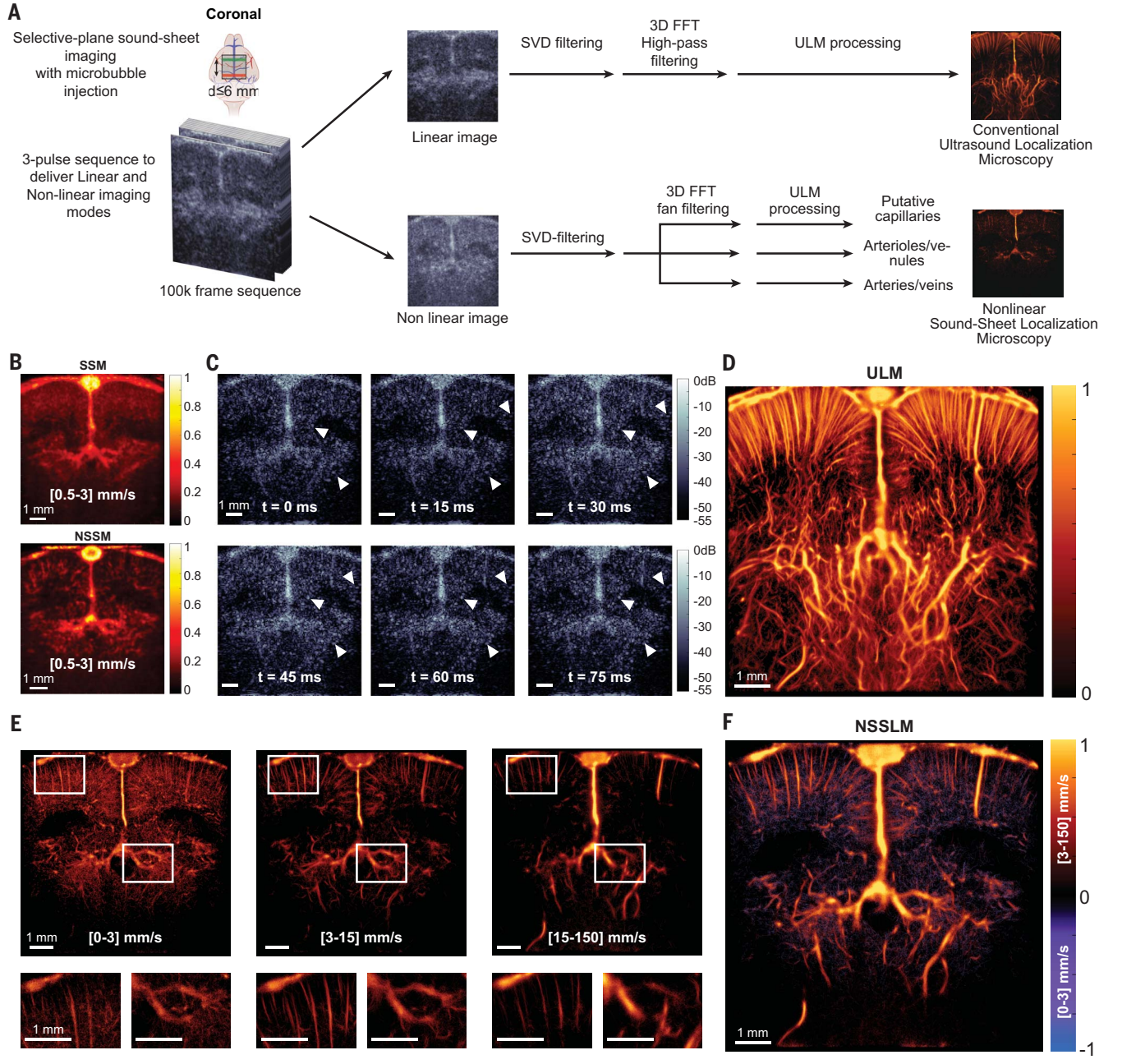

Fig. 5. Nonlinear sound-sheet localization microscopy of rat brain capillaries. (**A**) ULM and NSSLM image processing pipelines. (**B**) Vascular information captured by Doppler SSM and Doppler NSSLM in the capillary blood flow velocity band (0.5 to 3 mm/s). (**C**) NSSM frames of the NSSLM sequence revealing slow MB flow in the rat brain. White arrows indicate quasi-stationary MBs, and *t* represents the frame acquisition time. (**D**) ULM image generated with a state-of-the-art ULM processing pipeline (fig. S7). (**E**) (Top) NSSLM in the capillary flow velocity band (0.5 to 3 mm/s), arteriole and venule flow velocity band (3 to 15 mm/s), and artery and vein velocity band (15 to 150 mm/s). (Bottom) Zoomed-in views of white-boxed areas from above. (**F**) Composite NSSLM image display of all cerebral blood flow velocity bands.

of the sinus vein were visible in Doppler NSSM. Time series of NSSM frames filtered in the capillary velocity band (Fig. 5C) showed the dynamic of slow flowing MBs captured with NSSM, which constitutes the basis for NSSLM postprocessing. Individual microbubbles that are quasistatic are indicated with white arrows. Over the course of 75 ms, several MBs progressed by less than half a wavelength (57 μm), indicating that their velocities were below 0.8 mm/s, which falls in the range of capillary flow velocities.

As a reference, we processed a state-of-the-art ULM density map using X wave transmissions (Fig. 5D). In comparison, NSSLM (Fig. 5, E and F) enabled mapping of capillary beds segmented with a 0 to 3 mm/s flow velocity band (Fig. 5E, left), arterioles and venules segmented with a 3 to 15 mm/s flow velocity band (Fig. 5E, middle), and arteries and veins segmented with a 15 to 150 mm/s flow velocity band (Fig. 5E, right).

A composite NSSLM image showing all vascular compartments is presented in Fig. 5F. Vascular structures displayed in the NSSLM image appeared clearly denser than structures detected with ULM, as expected from capillary beds (*41*). The results for the second plane exhibit similar characteristics and are presented in figs. S8 and S9.

Discussion

We report NSSM, a fast and volumetric imaging method capable of visualizing targeted biological processes at the organ scale. NSSM introduces nonlinear sound-sheet beams in the field of ultrasound imaging and is capable of detecting two major classes of ultrasound contrast agents, genetically encoded GVs and intravascular MBs. Thanks to its all-acoustic nature, NSSM circumvents certain limitations of light-sheet or multiphoton microscopy (*3*, *46*, *47*), such as phototoxicity, photobleaching of fluorescent reporters, and complex single-objective microscope designs based on oblique illumination.

In two dimensions, NSSM achieved framerates of 4.4 kHz in thin sound sheets of 0.1 × 8.8 × 12.9 mm^3 or 1 × 89 × 130 λ^3. We show that sound-sheet beams can be arbitrarily positioned within the 8.8 × 8.8 mm^2 active aperture of a 15-MHz RCA transducer and swept electronically along each orthogonal array with a subwavelength precision of 55 μm (~λ/2).

NSSM can be further tuned for speed or spatial coverage. Inspired by multislice imaging of the brain (*48*), we report fast multiview NSSM at a frame rate of 1.7 kHz, enabling Doppler imaging of the rat brain. Symmetric planes in each brain hemisphere can be observed simultaneously and enable studies of lateralized brain function. Note that single- and multislice Doppler NSSM do not enable 4D ultrafast Doppler imaging because they are not illuminating the whole volume of view at once but rather subwavelength thin slices at a kilohertz frame rate. This multislice approach could be of interest to study vascular activity in a few predefined brain regions. One advantage of multislice Doppler NSSM compared with 4D Doppler imaging would be to significantly reduce the data rate.

The 64× increase in 2D imaging speed compared with xAM imaging enabled localization microscopy of the cerebral capillary vasculature. The combination of kilohertz imaging with specific MB detection regardless of MB velocity was fundamental to chart capillary territory and opens the way for imaging of microvascular activity deep in intact tissues. In this study, we acquired 2D super-resolution vascular images in parallel coronal planes spaced by several millimeters. Future work will investigate the feasibility of 3D NSSLM of the capillary vasculature using fast electronic sweeping of sound-sheet beams along adjacent planes spaced by half a wavelength.

Orthogonal NSSM microscanning enables volumetric imaging of genetically encoded bacterial and mammalian ARGs. In particular, 3D NSSM enabled longitudinal molecular ultrasound imaging of gene expression in a tumor model. The imaging method creates the possibility for in vivo tumor volume quantification in mammalian tissue. The high specificity of cross-amplitude modulation was critical to reveal the necrotic core of tumors, which classical pulse sequences would underestimate owing to nonlinear wave propagation artifacts.

Limitations

The imaging depth of SSM and NSSM are identical and limited by the cross-propagation depth z_{cp} (see materials and methods). For a transmitting aperture of 64 elements, an interelement spacing of 110 μm, and a cross-propagation angle α = 15°, z_{cp} ≈ 13 mm. NSSM imaging speed is limited by the speed of sound in two dimensions and by the speed of sound and the number of scanning steps in three dimensions. Theoretically, NSSM can reach 25,600 images/s and 233 volumes/s (table S1). The field of view of NSSM is limited by the size of the active surface of the transducer array. A 15-MHz RCA of 160 elements provides an accessible field of view of ~ 8.8 × 8.8 × 10 mm^3. A 15 MHz RCA of 256 elements would provide an accessible field of view of ~12.8 × 12.8 × 10 mm^3. For comparison purposes, the limits of 4D functional ultrasound neuroimaging reported in the literature (*18*) are a depth of 15 mm, a speed of 6 volumes/s, and a field of view of 9.6 × 9.6 × 15 mm^3.

Overall, the NSSM paradigm complements the capabilities of volumetric ultrasound imaging methods, such as functional ultrasound, orthogonal plane wave imaging (*22*), synthetic aperture imaging (*21*), or xDoppler (*49*), that provide anatomical or vascular information at the mesoscale but do not enable molecular or cellular imaging. In addition, 2D NSSM provides an improved resolution in elevation, which can be as low as 0.4 λ (*24*) versus ≥3 λ (*50*) for linear transducer arrays.

A limitation of NSSM is that the requirement for symmetric half-apertures to generate sound-sheet beams prevents imaging on the edge of the RCA transducer. However, orthogonal NSSM microscanning allows the retrieval of part of this missing volume such that the surface area lost in the corners of the active surface of the RCA transducer represents 11% (77.44 to 69.24 cm^2). In addition, wider RCA transducers made of 256 elements could be operated with our current hardware and would automatically increase the field of view.

Another limitation lies in the volumetric imaging rate achievable with SSM, which lies in the hundreds of hertz and not kilohertz. This volume rate remains comparable to other high-quality RCA volumetric imaging methods, such as functional orthogonal plane wave (OPW) neuroimaging (*51*) or synthetic aperture B-mode imaging (*52*). Compared with 2D ultrafast Doppler imaging based on tilted plane wave transmissions, Doppler NSSM requires the injection of nonlinear ultrasound contrast agents into the bloodstream. Both Doppler approaches rely on the continuous transmission of ultrasound waves at kilohertz frame rates. Doppler NSSM outperforms 2D ultrafast Doppler imaging in terms of resolution in elevation and detection of slow cerebral blood flows. Note that Doppler NSSM is not suited for 4D Doppler imaging because it is not insonifying the whole volume of view at once but rather subwavelength thin tissue sections. 4D ultrafast Doppler imaging has been implemented on RCA arrays using OPW transmissions (*51*).

A third limitation of our study is that brain imaging was performed in craniotomized animals. The transcranial potential of NSSM has not been explored. Additionally, NSSM will be compatible with chronic acoustic windows (*53*). In light of recent advances in transcranial ULM using fully addressed or RCA probes, we foresee that transcranial NSSLM will achieve a similar sensitivity to capillary flow as sensitivity arises from the NSSLM method itself.

NSSM would also benefit from the development of monodisperse MBs tuned for high-frequency ultrasound because it would improve CNR and allow us to reduce MB doses administered (*54*).

The performance of NSSM is also bound by the collapse pressure of ARGs. A trade-off exists between imaging depth that requires high acoustic pressures and near-field detection of ARGs that would be collapsed if high acoustic pressures are used.

We acknowledge that validation is a long-standing challenge for super-resolution ultrasound imaging in general and NSSLM of capillary beds in particular. NSSLM provides a combination of depth and resolution inaccessible to other in vivo techniques, making cross-referencing challenging. Hierarchical phase-contrast tomography at the European Synchrotron Radiation Facility (*55*) could serve as a comparison in the future.

Capillary flow velocities reported in this work are consistent with other studies (*40*), and MB entry and exit from capillaries could be observed by combining continuous NSSLM acquisitions at kilohertz frame rates with long-ensemble SVD filters. A significant advantage of NSSLM over conventional ULM is that sound-sheet imaging confines the echoes of intravascular microbubbles to a plane with a subwavelength resolution in elevation. This alleviates the risk of mapping out-of-plane vessels.

The combination of latest and future generation acoustic probes (*56*) with NSSM carries a wave of opportunities for deep tissue imaging of dynamic biological processes. NSSM offers an unprecedently high spatiotemporal resolution and coverage to explore living opaque organs across scales.

Materials and methods

Generation of nondiffractive ultrasound beams

RCA rows or columns were used to transmit simultaneous cross-propagating plane waves

from two contiguous half-apertures $\frac{N_{ap}}{2}$ at angles α and $-\alpha$ (Fig. 1B). The two transmitted plane waves interfere along a 2D plane, referred to as the sound-sheet plane. During cross-propagation, an X wave with a double amplitude is generated and propagates with a supersonic velocity $\frac{c_0}{\cos(\alpha)}$ until the cross-propagation depth $z_{cp} = \frac{N_{ap}}{2}\cot(\alpha)$. Ultrasound echoes received by the array orthogonal to the transmitting array are processed to generate an image. Image reconstruction relies on a delay-and-sum beamforming algorithm with the assumption that ultrasound backscattering only arises from the sound-sheet plane. For beamforming delay laws, see the image reconstruction paragraph and reference (*25*).

Subwavelength microscanning and 3D ultrasound imaging

Nondiffractive beams can be generated two ways (Fig. 1H). First, using two contiguous subapertures of RCA transducer elements. This focuses the sound-sheet plane at a position $x_{SS} = x_{p/2} = (n-1)p + \frac{p}{2}$, with n being the number of elements, and p being the pitch or interelement spacing of the RCA transducer. Second, using two subapertures of RCA transducer elements separated by an inactive element. This focuses the cross-propagation plane at a position $x_{SS} = x_p = np$. In practice, these two transmissions generate nondiffractive beams with main-lobes separated by a distance of $\frac{p}{2}$. The thickness of the sound sheet was estimated using iterative nonlinear contrast source (INCS) simulations (*25*), the full width at half maximum (FWHM) of the main lobe of the nondiffractive beam can be approximated with the following relation:

$$\mathrm{FWHM}_{SS} = \frac{0.32\lambda}{\sin(\alpha)}$$

In particular, the FWHM becomes smaller than the wavelength for any angle $\alpha > 18.66°$.

By performing sound-sheet microscanning in x and x, a volume is sampled. Note that sound-sheet microscanning can also be performed along only x or y. Because sound-sheets are generated using two half-apertures, the field of view FoV is reduced compared to active surface of the RCA transducer: $FoV = N_{total} \times p - 2 \times \frac{N_{ap}}{2}$. The volume occupied by the main lobe of a sound sheet beam is therefore: $z_{cp} \times FWHM_{SS} \times w_{array}$, with $w_{array} = N_{total}\ p$ the full width of the RCA array. Therefore, the volume of sound-sheet scan along one array is equal to:

$$z_{cp} \times N_{SS}\mathrm{FWHM}_{SS} \times w_{array}$$

with N_{SS} the number of sound sheet positions.

By using varying aperture sizes, it is possible to extend the field of view further, but then the propagation depth z_{cp} is reduced. To keep z_{cp} constant, one possibility is to decrease angle α. Considering a minimum half-aperture for sound-sheet transmission $N_{red}p$, the total field of view covered by a scan in one direction is:

$$z_{cp} \times (N_{total} - N_{red})p \times w_{array} =$$
$$z_{cp} \times w_{array}^2 - z_{cp} \times w_{array} \times N_{red}$$

and for a 3D scan along x and y, this becomes:

$$z_{cp} \times w_{array}^2 - 4(N_{red}p)^2$$

When compared to active surface of the RCA transducer, this leads to a field of view reduction of:

$$1 - \frac{z_{cp}(N_{total}^2 - 4N_{red}^2)p^2}{z_{cp}(N_{total}p)^2} = 4\frac{N_{red}^2}{N_{total}^2}$$

In our study, we used a reduced aperture of as low as 12 elements, leading to a 11% loss in image volume.

Spatial confinement of nonlinear scattering via amplitude modulation

In NSSM, the same half-apertures are used for two additional transmits, each firing independently this time (events TX2 and TX3, Fig. 1D). As no cross-propagation is taking place in this case, the acoustic pressure delivered along the sound-sheet plane has a twice lower amplitude than TX1. An amplitude-modulated signal can thus be obtained by subtracting echoes received from TX2 plus TX3 from echoes received from TX1. This operation is done on the radiofrequency data and the residual signal is beamformed and further processed. A 3D NSSM image can also be obtained by performing three xAM pulse transmissions for every sound-sheet position in x and y.

Sound-sheet image reconstruction

To reconstruct an image from the sound-sheet, we make the assumption that backscattered echoes originate only from the sound sheet plane. If the sound sheet plane is oriented with its normal along the $\vec{x}$ direction, then all scatterers can be assumed to have the same y coordinate. The forward delay for a scatterer at a position (x_s, y_s, z_s) can be written as:

$$t_f(x_s, y_s, z_s) = \frac{z_s}{c_{ss}} = \frac{z_s\cos(\alpha)}{c_0}$$

With c_{ss} the supersonic speed of the sound-sheet, and c_0 is the speed of sound in the medium.

The return delay for a scatterer at a position $(x_s, y_s,\ z_s)$ is calculated for the array orthogonal to the transmitting array to restore focusing and is written as:

$$t_r(x_s, y_s,\ z_s) = \frac{\sqrt{z_s^2 + y_s^2}}{c_0}$$

It is important to notice that t_f only depends on $z_s,\ x_s$, whereas t_r only depends on $z_s,\ y_s$.

Simulation of linear and nonlinear sound-sheet beams

Linear and nonlinear sound-sheet beams reported in Fig. 1, C and E, were computed with the INCS method (*25*). Briefly, INCS was developed to solve the four-dimensional spatiotemporal Westervelt equation describing nonlinear sound wave propagation. Simulations were conducted within a computational domain $x \times y \times z = 6.5 \times 13 \times 10.5\ \mathrm{mm}^3$. The propagation medium consisted of water and was characterized by a mass density $\rho_0 = 1060\ \mathrm{kg/m}^3$ and a speed of sound $c_0 = 1482$ m/s. The incident beam had a center frequency $f_c = 15$ MHz. The simulated RCA array consisted of 64 individual elements, each with a length of 12.88 mm and a pitch of 100 μm. The transmitted pulses were modeled as Gaussian-apodized sine bursts:

$$p(t) = P_{0exp}\left[-\left(\frac{t - T_d}{T_w/2}\right)^2\right]\sin[2\pi f_0(t - T_d)],$$

with $T_w = 1.5/f_c$ representing the duration of the Gaussian envelope, and $T_d = 3/f_c + \Delta_n$, a total time delay. The latter consists of a fixed delay for keeping $p(t = 0) \sim 0$, plus a delay per element for the beam steering. Beams are simulated for an angle $\alpha = 20.7°$. The peak acoustic pressure of the elements surface was $P_0 = 500$ kPa. A sampling frequency of 90 MHz was used to discretize the spatiotemporal domain.

Simulation of NSSM point spread functions

We simulated the response of four resonant microbubbles in a homogeneous water medium using the k-Wave simulation toolbox. MBs were positioned at $z = 1$, 2, 3, and 4 mm and centered in the middle of the domain. Each MB had a diameter of 1.5 μm, leading to a resonance frequency of 15.625 MHz. In this simulation, the geometry of the transducer consists of 43 elements with a height of 4.3 mm, a width of 100 μm, a pitch of100 μm, and a bandwidth of 14 to 22 MHz. Twenty-two sound-sheet transmissions were simulated with a scanning step of 50 μm, an angle $\alpha = 21°$, a four-cycle Gaussian-apodized sine burst, and an acoustic peak pressure of 400 kPa at the transducer surface. The radiofrequency data was beamformed using the delay-and-sum algorithm described above. For 3D imaging, we permuted simulation data to emulate data of the orthogonal array as our problem is symmetric.

Ultrasound imaging of a wire phantom

A 15 MHz RCA probe with 80+80 elements (Verasonics, Kirkland, WA, USA) with a pitch or interelement spacing of 110 μm was placed over a 3D wire phantom (model 055A from CIRS, VA, USA). The wires were oriented at an angle from the orientation of the rows and columns elements. SSM images were obtained using a 14° angle per array (2 transmits per voxel result) and a combination of [7°, 15°, 20°]

angles (6 transmits per voxel result). As reference, an orthogonal plane wave (OPW) acquisition with an angle of −18° was used (2 transmits per voxel result) and 2 × 32 transmits ranging from −21° to 21° (64 transmits per voxel result). Imaging results are reported in supplementary fig. S1. C-scans, i.e., images in the *xy* plane, reveal wires in diagonal. For the SSM case, microscanning was performed with a 55- μm step. In-plane images, i.e., *xz* scans, reveal a single wire cross section. Waveforms transmitted in both cases were 13.6 MHz, 0.5-cycles sine bursts.

NSSM performance compared with xAM imaging

Imaging speed: The gold standard for nondestructive imaging of acoustic reporter genes in a tissue context is a method called xAM. xAM image acquisition operates line by line (24). An image is typically formed of 64 image lines, and for each line, the three pulses of the amplitude modulation sequence are transmitted sequentially. In the end, the acquisition of one xAM image requires 3 × 64 pulse transmissions. In NSSM, cross-propagating plane waves transmitted using the long elements of a row-column array intersect along a plane. The acquisition of one 2D NSSM image requires only three pulse transmissions. 2D NSSM is therefore 64 times faster than 2D xAM.

Imaging volume: xAM imaging operates on linear arrays of transducer elements. The volume insonified by xAM is a function of the width of the ultrasound beam in elevation (off-plane direction). At 15 MHz, the thickness of the ultrasound beam is ~350 μm or 3.5 λ, as illustrated below (*50*) (fig. S2D). A typical xAM image has a width of 64 λ (64 image lines spaced by 1 λ), a depth of 1 cm or 100 λ, and an elevation of 3.5 λ. This leads to an insonified volume $V_{xAM} \cong 3.5 \times 64 \times 100\ \lambda^3$. In comparison, NSSM operates on an RCA array with an active surface of 8.8 × 8.8 mm. The imaging volume accessible is therefore $V_{NSSM} \cong 80 \times 80 \times 100\ \lambda^3$. The leads to a volume ratio $V_{NSSM} / V_{xAM} \cong 35$.

Ultrasound imaging of GV phantoms

Fig. 2A: *A. flos aquae* GVs were cultured and transferred to sterile separating funnels. Buoyant cells were separated from the growth media through natural flotation, and GVs were harvested after 48h of hypertonic lysis. A cycle of centrifugation and resuspension allows to purify the GVs further. A stock of *A. flos aquae* GVs was stripped of their GvpC protein layer with a 6-M urea solution to obtain nonlinearly scattering GVs (ΔGvpC GVs). A 2% agar phantom comprising 2-mm–diameter wells was casted using custom-printed molds and imprints. For each of the four wells, the concentration is increased starting with a concentration measured optically at OD = 0.5, OD = 1, OD = 1.5, and OD = 2. Images were obtained with the 15 MHz RCA transducer (Verasonics, Kirkland, WA, USA). Waveforms transmitted were 13.6 MHz, 0.5-cycle sine bursts. The X-wave angle α was set to 19°.

Fig. 2D: *E. coli* bacteria were grown for 20 hours at 37°C, 220 RPM flask shaking in a terrific broth medium with 0.5% arabinose, 0.2% glucose, and BME vitamins. In one case, plasmid pBAD-bARGSer was transferred to the *E. coli* strain (courtesy of Shapiro Lab, derived from plasmid Addgene #192473) via electroporation. These cells produced *Serratia* GVs that are constitutively nonlinear scatterers. Both bacterial populations were then transferred to the phantom.

Ultrasound imaging of a cancer model

All in vivo experiments were performed under protocol 1761, approved by the Institutional Animal Care and Use of Committee of the California Institute of Technology. Animals were housed in a facility maintained at 71° to 75°F and 30 to 70% humidity, with a lighting cycle of 13 hours on and 11 hours off (light cycle 6:00 to 19:00). Tumor xenograft experiments were conducted in NSG mice aged 12 weeks and 6 days (Jackson Laboratory). As we relied on an orthotopic model of breast cancer, all mice were female. MDA-MB-231-mARGAna cells were grown in T225 flasks in DMEM supplemented with 10% TET-free FBS and penicillin–streptomycin until confluency as described above. Cells were harvested by trypsinization with 6 ml of trypsin/EDTA for 6 minutes and quenched with fresh media. Cells were washed once in DMEM without antibiotics or FBS before pelleting by centrifugation at 300G. Cell pellets were resuspended in a 1:1 mixture of ice-cold Matrigel (HC, GFR) (Corning, 354263) and PBS (Ca^{2+}, Mg2+-free) at 30 million cells per milliliter. Then, 50-μl Matrigel suspensions were injected bilaterally into the 4th mammary fat pads at 1.5 million cells per tumor by subcutaneous injection. Twelve hours after tumor injection and every 12 hours thereafter (except the mornings of ultrasound imaging sessions), test mice were intraperitoneally injected with 150 μl of saline containing 150 μg of doxycycline for induction of GV expression.

The 15 MHz RCA probe was operated to transmit pulses at 110 sound-sheets positions along each array, so 220 positions in total. For each sound-sheet position, waves were transmitted using seven angles ranging from 15° to 21° with steps of 1°. For each sound-sheet position, the three pulses of the sequence were transmitted for the first angle, then the three pulses of the sequence were transmitted again for the next angle and so on until the last angle was reached. Then, the same set of transmit events was used for the next sound-sheet position. Scanning started on array 1 made of piezo-elements 1 to 80 and continued on array 2 made of piezo-elements 81 to 160. All 3D renderings were generated using the Avizo rendering software (ThermoFisher ®). To segment and measure the tumor and hypoxic core, the data was first 3D-Gaussian filtered (standard deviation σ = 0.6) and interpolated twice in each direction. The data was then normalized and log-compressed, and tissue attenuation was taken into account with an average tissue attenuation factor of 0.54 dB/MHz/cm. Attenuation was further corrected to aim for a uniform noise contrast value through depth of the image. The resulting volumes were filtered using a 3D Gaussian kernel with a standard deviation of σ = 50, and an isotropic size of 21 pixels was added prebinarization to yield better results. Then, a 2D binarized image is created by calculating global image threshold using Otsu's method controlled by a threshold luminance value set for each of the directions and each of the mice. The open volume result was then closed and measured using the regionprops function in Matlab (The Mathworks Inc, Natick, MA, USA). Tumor and necrotic core volumes were estimated three times out of each 3D NSSM scan. Two estimates were calculated out of sound sheet microscanning in the *x* and *y* direction respectively. After compounding volumetric data in the *x* and *y* direction, we estimated tumor and necrotic core volumes a third time by detecting contours of gene expression digitally in the *z* direction. With this approach, we calculated an average value for the volume of the tumor and hypoxic core presented in Fig. 3D.

Ultrasound Doppler imaging

The RCA probe was used to image the vascular function of a rat brain (Sprague Dawley, female, 280 g). All experiments were performed under CCD license number AVD8010020209725 at the Koninklijke Nederlandse Akademie van Wetenschappen with Study Dossier number 213601. Immediately after isoflurane induction, carprofen, and butorphanol were delivered subcutaneously. The animal was prepared (shaved, disinfected, placed in earbars) and surgery began no sooner than 20 min after injections. A catheter was placed in the tail vein. Heparin was injected to prevent blood clots forming in the catheter. 14 × 14 mm craniotomies were performed. Carprofen and butorphanol were delivered subcutaneously during surgery (respectively 5 and 2 mg/kg). To prevent cerebral edema, dexamethasone was given subcutaneously with a dosage of 2.5 mg/kg.

After craniotomy, the RCA probe was positioned over the cranial window of anesthetized animal. Sound-sheet were transmitted with an 18° angle, and 38 elements were used for each half apertures. The transmitted pulses were two-cycle sine bursts centered at 15.6 MHz. For Fig. 4C, 2100 frames were acquired with a frame rate of 4400 Hz. For Fig. 4D, 2100 frames

were acquired with a frame rate of 300 Hz, leading to a 7-s-long acquisition. For Fig. 4, G and H, 2100 frames were acquired with a frame rate of 1700Hz, leading to a 1.24-s-long acquisition. The average heart rate throughout the experiment is 419 bpm, leading to a cardiac cycle of 143 ms ,which is short enough to be captured several times in our acquisition. In these experiments, 1.0×10^8 microbubbles (Micromarker® Fujifilm, Bracco) were injected in a bolus through a tail vein catheter.

The structural similarity index matrix (SSIM) is calculated as:

$$\mathrm{SSIM}(x,y) = \frac{(2\mu_x\mu_y + C_1)(2\sigma_{xy} + C_2)}{\left(\mu_x^2 + \mu_y^2 + C_1\right)\left(\sigma_x^2 + \sigma_y^2 + C_2\right)}$$

where μ_x, μ_y, σ_x, σ_y, and σ_{xy} are the local means, standard deviations, and cross-covariance for images x, y, obtained from the intensity images after beamforming, and C_1, C_2 are regularization constants for luminance and contrast. The SSIM in Fig. 4E is calculated from the three adjacent frames. The asterisks show statistical significance using t test of two independent samples (P values are all $<10^{-21}$) (***$P < 0.001$; ****$P < 0.0001$).

For Fig. 4, F to J, three pulses were transmitted at sound sheet position 1 with a time between pulses set at 89 μs. These pulses were next transmitted at sound sheet position 2. This sequence was repeated to acquire data for Doppler processing in two separate planes. A total of 2100 frames was acquired per sound sheet position with a frame rate of 1700 Hz, leading to a 1.24-s-long acquisition. The average heart rate throughout the experiment was ranging from 300 to 360 bpm, leading to a cardiac cycle of 166 to 200 ms, which is short enough to be covered in between six to eight times during our acquisition. Here as well, 1.0×10^8 microbubbles (Micromarker® Fujifilm, Bracco) were injected in a bolus through a vein catheter.

Super-resolution ultrasound imaging

For the ULM and NSSLM experiments, similar surgical procedure and ultrasound pulse sequences were used than in the previous section. Ultrasound acquisitions were performed at a 1 kHz in two sound-sheet planes, recordings were continuous and lasted 105 s. Radio-frequency data for NSSLM was first filtered using the xAM operation and frames were beamformed using a delay-and-sum algorithm. Two independent post-processing pipelines were used to generate state-of-the-art ULM images and NSSLM images (fig. S7).

For ULM, the 1-lag cross-correlation is computed from the beamformed images, and then an adaptive TGC is computed and applied. MB echoes were retrieved using an SVD filter with a cutoff of 2 singular values. Using a 3D FFT fan filter, the resulting data are filtered in the temporal frequency domain: a hard-cutoff is implemented to get rid of low-frequency components (*57*–*60*). The data are then processed to detect microbubbles with respect to their intensity, and then a radial symmetry localization algorithm was applied, followed by Kuhn Munkres pairing for trajectory reconstruction (*43*).

For NSSLM, signal processing consisted in first filtering MB echoes with the amplitude modulation step of NSSM. Second, to increase the signal-to-noise ratio and compensate for attenuation, the 1-lag cross-correlation of the AM signal was computed and the signal was further adjusted using an adaptive time gain compensation function. To remove residual nonlinear tissue signals, a singular value decomposition clutter filter was applied with a cut-off of one singular value. Lastly, a 3D-FFT fan filter was implemented in the spatiotemporal frequency domain, and the signal was decomposed in the following velocity bands: 0 to 3, 3 to 15, 15 to 25, 25 to 60, and 60 to 150 mm/s (*57*–*60*). The imaging dataset was transformed back to the spatiotemporal domain, and MBs were localized using the radial symmetry algorithm (*42*). Individual MBs were paired with the Kuhn-Munkres assignment to retrieve MB trajectories. For the composite rendering of NSSLM, two color scales are applied based on different velocity domains.

REFERENCES AND NOTES

1. Method of the Year 2014. *Nat. Methods* **12**, 1 (2015). doi: 10.1038/nmeth.3251
2. V. Voleti *et al.*, Real-time volumetric microscopy of in vivo dynamics and large-scale samples with SCAPE 2.0. *Nat. Methods* **16**, 1054–1062 (2019). doi: 10.1038/s41592-019-0579-4; pmid: 31562489
3. B. Yang *et al.*, DaXi-high-resolution, large imaging volume and multi-view single-objective light-sheet microscopy. *Nat. Methods* **19**, 461–469 (2022). doi: 10.1038/s41592-022-01417-2; pmid: 35314838
4. K. McDole *et al.*, In Toto Imaging and Reconstruction of Post-Implantation Mouse Development at the Single-Cell Level. *Cell* **175**, 859–876.e33 (2018). doi: 10.1016/j.cell.2018.09.031; pmid: 30318151
5. J. Huisken, J. Swoger, F. Del Bene, J. Wittbrodt, E. H. K. Stelzer, Optical sectioning deep inside live embryos by selective plane illumination microscopy. *Science* **305**, 1007–1009 (2004). doi: 10.1126/science.1100035; pmid: 15310904
6. P. J. Keller, A. D. Schmidt, J. Wittbrodt, E. H. K. Stelzer, Reconstruction of zebrafish early embryonic development by scanned light sheet microscopy. *Science* **322**, 1065–1069 (2008). doi: 10.1126/science.1162493; pmid: 18845710
7. E. H. K. Stelzer *et al.*, Light sheet fluorescence microscopy. *Nat. Rev. Methods Primers* **1**, 73 (2021). doi: 10.1038/s43586-021-00069-4
8. P. P. Laissue, R. A. Alghamdi, P. Tomancak, E. G. Reynaud, H. Shroff, Assessing phototoxicity in live fluorescence imaging. *Nat. Methods* **14**, 657–661 (2017). doi: 10.1038/nmeth.4344; pmid: 28661494
9. V. Ntziachristos, Going deeper than microscopy: The optical imaging frontier in biology. *Nat. Methods* **7**, 603–614 (2010). doi: 10.1038/nmeth.1483; pmid: 20676081
10. E. M. Hillman *et al.*, High-speed 3D imaging of cellular activity in the brain using axially-extended beams and light sheets. *Curr. Opin. Neurobiol.* **50**, 190–200 (2018). doi: 10.1016/j.conb.2018.03.007; pmid: 29642044
11. F. F. Voigt *et al.*, The mesoSPIM initiative: Open-source light-sheet microscopes for imaging cleared tissue. *Nat. Methods* **16**, 1105–1108 (2019). doi: 10.1038/s41592-019-0554-0; pmid: 31527839
12. M. G. Shapiro *et al.*, Biogenic gas nanostructures as ultrasonic molecular reporters. *Nat. Nanotechnol.* **9**, 311–316 (2014). doi: 10.1038/nnano.2014.32; pmid: 24633522
13. D. Maresca *et al.*, Biomolecular Ultrasound and Sonogenetics. *Annu. Rev. Chem. Biomol. Eng.* **9**, 229–252 (2018). doi: 10.1146/annurev-chembioeng-060817-084034; pmid: 29579400
14. B. Heiles, D. Terwiel, D. Maresca, The Advent of Biomolecular Ultrasound Imaging. *Neuroscience* **474**, 122–133 (2021). pmid: 33727074
15. R. W. Bourdeau *et al.*, Acoustic reporter genes for noninvasive imaging of microorganisms in mammalian hosts. *Nature* **553**, 86–90 (2018). doi: 10.1038/nature25021; pmid: 29300010
16. A. Farhadi, G. H. Ho, D. P. Sawyer, R. W. Bourdeau, M. G. Shapiro, Ultrasound imaging of gene expression in mammalian cells. *Science* **365**, 1469–1475 (2019). doi: 10.1126/science.aax4804; pmid: 31604277
17. A. Lakshmanan *et al.*, Preparation of biogenic gas vesicle nanostructures for use as contrast agents for ultrasound and MRI. *Nat. Protoc.* **12**, 2050–2080 (2017). doi: 10.1038/nprot.2017.081; pmid: 28880278
18. C. Brunner, Grillet, A platform for brain-wide functional ultrasound imaging and analysis of circuit dynamics in behaving mice. *Neuron* **108**, 29 (2020). doi: 10.1016/j.neuron.2020.09.020
19. C. Rabut *et al.*, 4D functional ultrasound imaging of whole-brain activity in rodents. *Nat. Methods* **16**, 994–997 (2019). doi: 10.1038/s41592-019-0572-y; pmid: 31548704
20. B. Heiles *et al.*, Volumetric ultrasound localization microscopy of the whole rat brain microvasculature. *IEEE Open J. Ultrason. Ferroelectr. Freq. Control* **2**, 261 (2022). doi: 10.1109/OJUFFC.2022.3214185
21. M. F. Rasmussen, T. L. Christiansen, E. V. Thomsen, J. A. Jensen, 3-D imaging using row-column-addressed arrays with integrated apodization - part i: Apodization design and line element beamforming. *IEEE Trans. Ultrason. Ferroelectr. Freq. Control* **62**, 947–958 (2015). doi: 10.1109/TUFFC.2014.006531; pmid: 25974918
22. M. Flesch *et al.*, 4D *in vivo* ultrafast ultrasound imaging using a row-column addressed matrix and coherently-compounded orthogonal plane waves. *Phys. Med. Biol.* **62**, 4571–4588 (2017). doi: 10.1088/1361-6560/aa63d9; pmid: 28248655
23. J. A. Jensen *et al.*, Anatomic and Functional Imaging Using Row-Column Arrays. *IEEE Trans. Ultrason. Ferroelectr. Freq. Control* **69**, 2722–2738 (2022). doi: 10.1109/TUFFC.2022.3191391; pmid: 35839193
24. D. Maresca, D. P. Sawyer, G. Renaud, A. Lee-Gosselin, M. G. Shapiro, Nonlinear X-wave ultrasound imaging of acoustic biomolecules. *Phys. Rev. X* **8**, 041002 (2018). doi: 10.1103/PhysRevX.8.041002; pmid: 34040818
25. A. Matalliotakis, R. Waasdorp, M. D. Verweij, D. Maresca, Impact of wavefront shape on nonlinear ultrasound imaging of monodisperse microbubbles. *Phys. Rev. Appl.* **22**, 034062 (2024). doi: 10.1103/PhysRevApplied.22.034062
26. A. Lakshmanan *et al.*, Acoustic biosensors for ultrasound imaging of enzyme activity. *Nat. Chem. Biol.* **16**, 988–996 (2020). doi: 10.1038/s41589-020-0591-0; pmid: 32661379
27. A. Bar-Zion *et al.*, Acoustically triggered mechanotherapy using genetically encoded gas vesicles. *Nat. Nanotechnol.* **16**, 1403–1412 (2021). doi: 10.1038/s41565-021-00971-8; pmid: 34580468
28. R. C. Hurtetal., Genomically mined acoustic reporter genes enable real-time *in vivo* monitoring of tumors and tumor-homing probiotics. bioRxiv 2021.04.26.441537 [Preprint] (2022); https://doi.org/10.1101/2021.04.26.441537.
29. S. Nagai, K. Iizuka, A practical ultrasound axicon for non-destructive testing. *Ultrasonics* **20**, 265–270 (1982). doi: 10.1016/0041-624X(82)90047-6
30. T.-Y. Lai, M. Bruce, M. A. Averkiou, Modeling of the Acoustic Field Produced by Diagnostic Ultrasound Arrays in Plane and Diverging Wave Modes. *IEEE Trans. Ultrason. Ferroelectr. Freq. Control* **66**, 1158–1169 (2019). doi: 10.1109/TUFFC.2019.2908831; pmid: 30951464
31. D. Maresca *et al.*, Nonlinear ultrasound imaging of nanoscale acoustic biomolecules. *Appl. Phys. Lett.* **110**, 073704 (2017). doi: 10.1063/1.4976105; pmid: 28289314
32. B. Heiles, D. Maresca; Delft University of Technology, Nonlinear sound-sheet microscopy: imaging opaque organs at the capillary and cellular scale, Zenodo (2024); https://doi.org/10.5281/zenodo.13988115.
33. A. Courbet, D. Endy, E. Renard, F. Molina, J. Bonnet, Detection of pathological biomarkers in human clinical samples via amplifying genetic switches and logic gates. *Sci. Transl. Med.* **7**, 289ra83 (2015). doi: 10.1126/scitranslmed.aaa3601; pmid: 26019219

34. M. Versluis, E. Stride, G. Lajoinie, B. Dollet, T. Segers, Ultrasound Contrast Agent Modeling: A Review. *Ultrasound Med. Biol.* **46**, 2117–2144 (2020). doi: 10.1016/j.ultrasmedbio.2020.04.014; pmid: 32546411
35. G. Renaud, J. G. Bosch, A. F. W. van der Steen, N. de Jong, Increasing specificity of contrast-enhanced ultrasound imaging using the interaction of quasi counter-propagating wavefronts: A proof of concept. *IEEE Trans. Ultrason. Ferroelectr. Freq. Control* **62**, 1768–1778 (2015). doi: 10.1109/TUFFC.2015.007169; pmid: 26470039
36. E. Mace *et al*., Functional ultrasound imaging of the brain: Theory and basic principles. *IEEE Trans. Ultrason. Ferroelectr. Freq. Control* **60**, 492–506 (2013). doi: 10.1109/TUFFC.2013.2592; pmid: 23475916
37. C. Demené *et al*., Spatiotemporal Clutter Filtering of Ultrafast Ultrasound Data Highly Increases Doppler and fUltrasound Sensitivity. *IEEE Trans. Med. Imaging* **34**, 2271–2285 (2015). doi: 10.1109/TMI.2015.2428634; pmid: 25955583
38. C. Tremblay-Darveau, R. Williams, L. Milot, M. Bruce, P. N. Burns, Combined perfusion and doppler imaging using plane-wave nonlinear detection and microbubble contrast agents. *IEEE Trans. Ultrason. Ferroelectr. Freq. Control* **61**, 1988–2000 (2014). doi: 10.1109/TUFFC.2014.006573; pmid: 25474775
39. C. Errico *et al*., Ultrafast ultrasound localization microscopy for deep super-resolution vascular imaging. *Nature* **527**, 499–502 (2015). doi: 10.1038/nature16066; pmid: 26607546
40. S. Lee *et al*., Functional Assessment of Cerebral Capillaries using Single Capillary Reporters in Ultrasound Localization Microscopy. arXiv:2407.07857 [physics.med-ph] (2024).
41. C. Kirst *et al*., Mapping the Fine-Scale Organization and Plasticity of the Brain Vasculature. *Cell* **180**, 780–795.e25 (2020). doi: 10.1016/j.cell.2020.01.028; pmid: 32059781
42. B. Heiles *et al*., Performance benchmarking of microbubble-localization algorithms for ultrasound localization microscopy. *Nat. Biomed. Eng.* **6**, 605–616 (2022). doi: 10.1038/s41551-021-00824-8; pmid: 35177778
43. H. W. Kuhn, The Hungarian method for the assignment problem. *Nav. Res. Logist. Q.* **2**, 83–97 (1955). doi: 10.1002/nav.3800020109
44. D. Kleinfeld, P. P. Mitra, F. Helmchen, W. Denk, Fluctuations and stimulus-induced changes in blood flow observed in individual capillaries in layers 2 through 4 of rat neocortex. *Proc. Natl. Acad. Sci. U.S.A.* **95**, 15741–15746 (1998). doi: 10.1073/pnas.95.26.15741; pmid: 9861040
45. S. K. Piechnik, P. A. Chiarelli, P. Jezzard, Modelling vascular reactivity to investigate the basis of the relationship between cerebral blood volume and flow under CO2 manipulation. *Neuroimage* **39**, 107–118 (2008). doi: 10.1016/j.neuroimage.2007.08.022; pmid: 17920935
46. B.-C. Chen *et al*., Lattice light-sheet microscopy: Imaging molecules to embryos at high spatiotemporal resolution. *Science* **346**, 1257998 (2014). doi: 10.1126/science.1257998; pmid: 25342811
47. N. G. Horton *et al*., *In vivo* three-photon microscopy of subcortical structures within an intact mouse brain. *Nat. Photonics* **7**, 205–209 (2013). doi: 10.1038/nphoton.2012.336; pmid: 24353743
48. D. A. Feinberg, K. Setsompop, Ultra-fast MRI of the human brain with simultaneous multi-slice imaging. *J. Magn. Reson.* **229**, 90–100 (2013). doi: 10.1016/j.jmr.2013.02.002; pmid: 23473893
49. A. Bertolo, J. Sauvage, M. Tanter, M. Pernot, T. Deffieux, XDoppler: Cross-correlation of orthogonal apertures for 3D blood flow imaging. *IEEE Trans. Med. Imaging* **40**, 3358–3368 (2021). doi: 10.1109/TMI.2021.3084865; pmid: 34048341
50. É. Macé *et al*., Whole-Brain Functional Ultrasound Imaging Reveals Brain Modules for Visuomotor Integration. *Neuron* **100**, 1241–1251.e7 (2018). doi: 10.1016/j.neuron.2018.11.031; pmid: 30521779
51. J. Sauvage *et al*., 4D Functional Imaging of the Rat Brain Using a Large Aperture Row-Column Array. *IEEE Trans. Med. Imaging* **39**, 1884–1893 (2020). doi: 10.1109/TMI.2019.2959833; pmid: 31841403
52. J. A. Jensen *et al*., "Synthetic Aperture High Quality B-mode Imaging with a Row-Column Array Compared to Linear Array Imaging" presented at the 2022 IEEE International Ultrasonics Symposium (IUS), Venice, Italy, 10 to 13 October 2022 (IEEE, 2022), pp. 1–4; https://ieeexplore.ieee.org/document/9957973/.
53. B. J. Edelman *et al*., The COMBO window: A chronic cranial implant for multiscale circuit interrogation in mice. *PLoS Biol.* **22**, e3002664 (2024).
54. T. Segers *et al*., Monodisperse Versus Polydisperse Ultrasound Contrast Agents: Non-Linear Response, Sensitivity, and Deep Tissue Imaging Potential. *Ultrasound Med. Biol.* **44**, 1482–1492 (2018). doi: 10.1016/j.ultrasmedbio.2018.03.019; pmid: 29705522
55. Y. Jain *et al*., Vasculature segmentation in 3D hierarchical phase-contrast tomography images of human kidneys. [Preprint] (2024). https://doi.org/10.1101/2024.08.25.609595.
56. Z. Jin *et al*., Ultrasonic reporters of calcium for deep tissue imaging of cellular signals. bioRxiv 2023.11.09.566364 [Preprint] (2023); https://doi.org/10.1101/2023.11.09.566364.
57. C. Huang *et al*., Short Acquisition Time Super-Resolution Ultrasound Microvessel Imaging via Microbubble Separation. *Sci. Rep.* **10**, 6007 (2020). doi: 10.1038/s41598-020-62898-9; pmid: 32265457
58. G. Koukiou, V. Anastassopoulos, Velocity Filter Banks using 3-D FFT. (2013).
59. G. Koukiou, V. Anastassopoulos, Velocity Filtering Using Quantum 3D FFT. *Photonics* **10**, 483 (2023). doi: 10.3390/photonics10050483
60. A. Kojima, N. Sakurai, J. I. Kishigami, "Motion detection using 3D-FFT spectrum" presented at *1993 IEEE International Conference on Acoustics, Speech, and Signal Processing*, Minneapolis, MN, USA, 27 to 30 April 1993 (IEEE, 1993), pp. 213–216; https://ieeexplore.ieee.org/document/319785/.

ACKNOWLEDGMENTS

The authors thank members of the Shapiro and Maresca laboratories for helpful discussions as well as V. Galligioni, G. de Fluiter, and veterinary staff of the Netherlands Institute of Neuroscience for their continuous support. **Funding:** Delft University Fund (D.M.); 4TU Precision Medicine Program (D.M.); Dutch Research Council (D.M.); Chan Zuckerberg Initiative Dynamic RFA number 2023-321233 (D.M.); Marie-Sklodowska Curie Fellowship MIC-101032769 (B.H.); National Institutes of Health grant R01-EB018975 (M.G.S.); Chan Zuckerberg Initiative Deep Tissue Imaging RFA (M.G.S.); Howard Hughes Medical Institute (M.G.S.). **Author contributions:** Conceptualization: B.H., D.M. Methodology: B.H., F.N., D.T., B.M.P., T.A., P.B.L., M.D., D.M. Software: B.H., R.W., A.M. Investigation: B.H., F.N., R.W., E.M.I., P.B.L., M.D. Visualization: B.H. Funding acquisition: B.H., M.G.S., V.G., D.M. Project administration: B.H., D.M. Supervision: D.M. Writing – original draft: B.H., D.M. Writing – review & editing: B.H., M.G.S., V.G., D.M. **Competing interests:** B.H. and D.M. have a pending patent application concerning this technology: "Sound Sheet Imaging," OCNL application number NL 2035960, Technische Universiteit Delft (2023). B.H. is a coinventor on patent "Portable Imaging System," application number 18/566,843, publication number 20240268791, filed on 3 June 2022. M.G.S. is an inventor on patents pertaining to acoustic reporter genes filed by the California Institute of Technology. The other authors declare that they have no competing interests. **Data and materials availability:** NSSM acquisition and processing scripts are available on Github (https://github.com/MarescaRenaudLabs/NSSM), the computational NSSLM processing pipeline is hosted on Github (https://github.com/MarescaRenaudLabs/NSSLM), and all NSSM and NSSLM data and code are archived at Zenodo (*32*).

SUPPLEMENTARY MATERIALS

science.org/doi/10.1126/science.ads1325
Figs. S1 to S9
Table S1
MDAR Reproducibility Checklist

Submitted 31 July 2024; accepted 31 January 2025
10.1126/science.ads1325